

Analysis of Payload Fairing and Payload Adaptor of GSLV (Geosynchronous Satellite Launch Vehicle)

Project Report for Indian Institute of Technology, Bombay - AE238: Aerospace Structural Mechanics (2023)

Yashodhan Atul Tingne

Dept. of Aerospace Engineering

Indian Institute of Technology, Bombay

Mumbai, Maharashtra

210010065@iitb.ac.in

Parsana Vivek Navinbhai

Dept. of Aerospace Engineering

Indian Institute of Technology, Bombay

Mumbai, Maharashtra

210010047@iitb.ac.in

Bagadiya Keyur

Dept. of Aerospace Engineering

Indian Institute of Technology, Bombay

Mumbai, Maharashtra

210010019@iitb.ac.in

Sahil Nitin Kale

Dept. of Aerospace Engineering

Indian Institute of Technology, Bombay

Mumbai, Maharashtra

210010054@iitb.ac.in

Vivek Grover

Dept. of Aerospace Engineering

Indian Institute of Technology, Bombay

Mumbai, Maharashtra

210010075@iitb.ac.in

I. ABSTRACT

GSLV mark-3 is a significant step for India's space ambitions as it is the first step toward India's ambition to send Indian astronauts into space. It is also significant from the perspective of ISRO's own cryogenic engine. It proved ISRO's maturity in reentry technology, and its ability to develop braking techniques, deceleration technology, and thermal protection system for crew modules. The new launch vehicle is named the LVM-3 or Geostationary satellite launch vehicle MK. 3 is the most capable rocket developed by India. It can carry up to 4 metric tons 8800 pounds into geostationary transfer orbit once it is operational, a milestone Indian officials hope to achieve within two years.

To achieve low-cost access to space, ISRO has chalked down a plan to develop a new breed of reusable launch system called AVATAR to substantially cut down the launch costs. AVATAR will be a Single Stage Ro Orbit(SSTO) launch system that will attempt to reuse maximum sub-systems and will use turbojet and dual mode ramjet-scramjet propulsion. SSTO launch system will take a long time to develop. Accordingly, ISRO has decided to first develop a Two-stage to Orbit(TSTO) reusable launch system for the immediate future by utilizing its current capabilities and target development of AVATAR in the long term.

II. INTRODUCTION

The Geosynchronous Satellite Launch Vehicle, usually known by its abbreviation GSLV, is an expendable launch system developed to enable India to launch its INSAT-type satellites into geostationary orbit and to make India less dependent on foreign rockets. At present, it is ISRO's second-heaviest satellite launch vehicle and is capable of putting a total payload of up to 5 tons to Low Earth Orbit. The vehicle

is built by India with the cryogenic engine purchased from Russia while the ISRO develops its own engine programme.

In a setback for ISRO, the attempt to launch the GSLV, GSLV-F07 carrying GSAT-5P, failed on 25 December 2010. The initial evaluation implies that loss of control for the strap-on boosters caused the rocket to veer from its intended flight path, forcing a programmed detonation. Sixty-four seconds into the first stage of flight, the rocket began to break up due to the acute angle of attack. The body housing the 3rd stage, the cryogenic stage, incurred structural damage, forcing the range safety team to initiate a programmed detonation of the rocket.

On 5 January 2014, GSLV-D5 successfully launched GSAT-14 into intended orbit. This also marked first successful flight using indigenous cryogenic engine, making India the sixth country in the world to have this technology.

GSLV-Mk III can launch four tonne satellite into geosynchronous transfer orbit. It is a three-stage vehicle with a 110 tonne core liquid propellant stage (L-110) and a strap-on stage with two solid propellant motors, each with 200 tonne propellant (S-200). The upper stage will be cryogenic with a propellant loading of 25 tonne (C-25). It has a lift-off mass of about 640 tonnes, and is 43.43 meters tall. The payload fairing has a diameter of 5 meters and a payload volume of 100 cubic meters. It will allow India to become less dependent on foreign rockets for heavy lifting.

On 18 December 2014, ISRO successfully conducted an experimental test-flight of GSLV MK III carrying a crew module, to be used in future human space missions. This suborbital test flight demonstrated the performance of GSLV Mk III in the atmosphere.

A payload fairing is a nose cone used to protect a spacecraft's payload against the impact of dynamic pressure and

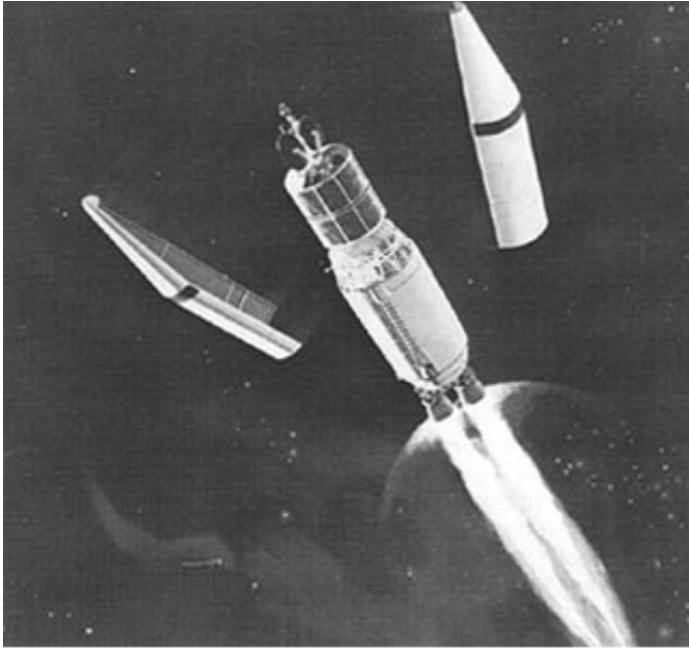


Fig. 1. Payload Fairing

aerodynamic heating during launch through an atmosphere. On some flights, another function is maintaining the clean-room environment for precision instruments. Once outside the atmosphere, the fairing is jettisoned, exposing the payload to outer space.

In GSLV, the payload fairing, 7.8 m (26 ft) long and 3.4 m (11 ft) in diameter, protects the vehicle electronics and the spacecraft during its ascent through the atmosphere. It is discarded when the vehicle reaches an altitude of about 115 km (71 mi).

The fourth operational flight of GSLV Mark I, GSLV-F06, had a more prolonged third stage called the C15 with 15-tonne propellant loading and employed a 4-meter diameter payload fairing.

Spacecraft that are designed to be injected into an orbit by a launch vehicle have different shapes and dimensions. To cater for these differences, the attachment of the spacecraft or satellite to the rocket launcher structure is normally performed through an adapter. There are various designs of the space adapters [1-3]. Some of the most commonly used designs are shown in Fig. 1. These include the frame-based design (see Fig. 1a), conical shell (see Fig. 1b), and conical lattice structure (see Fig. 1c).

The payload adapter was the physical structure used to connect the orbiter to the launch vehicle. The spacecraft was mounted on the Centaur using a 1,194-millimeter-diameter (47-inch) Payload Adapter. A clamp band secured the spacecraft to the launch vehicle. When the launch vehicle mission was complete, the Centaur released the clamp band, and the spacecraft separated from the launch vehicle using "push-off" springs.

Major loadings are applied to the adapter structure during

the injection of the payload into an orbit. The intensity of these loadings depends on the mass of the payload and the longitudinal and transverse g-forces. To withstand these loads the adapter should have an appropriate stiffness with the minimal mass. These requirements call for new efficient designs of the adapters to be developed. In this work, a number of new adapter designs are proposed and analysed. Using finite-element models, effects of geometry parameters on the critical buckling forces and moments, and frequencies of axial and transverse vibrations are investigated.

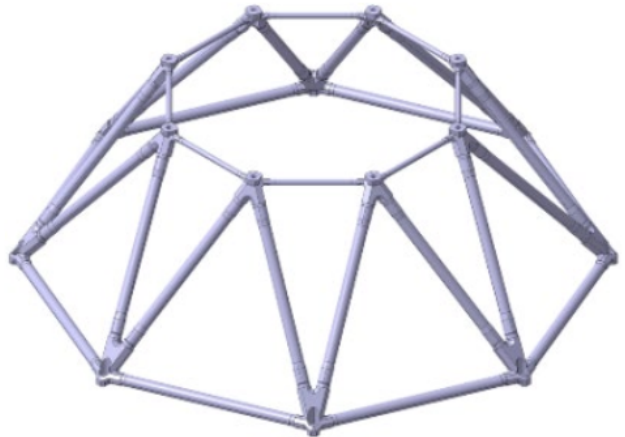


Fig. 2. Payload Adaptor 1

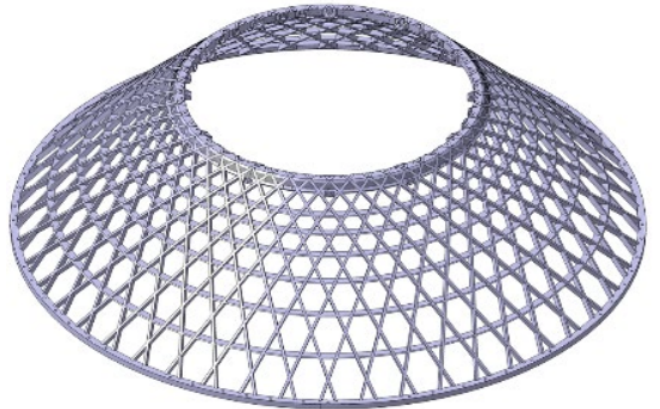


Fig. 3. Payload Adaptor 2

III. AERODYNAMIC STUDY OF PAYLOAD FAIRING

A. Pressure Distribution and Shock Location

- There is a discontinuity in the surface curvature at various junctions of the PLF. This discontinuity affects the pressure distribution. The Mach number at the approach to the nose cap is in the subsonic region. As the flow approaches the nose cap, stagnation point is formed.

The velocity at this stagnation point is zero. After this point, the flow accelerates as it flows along the nose cone and eventually becomes subsonic till it reaches the nose cylinder junction. The flow attempts to regain free stream properties as it now flows along the cylinder. The approach Mach number is responsible for affecting the flow behaviour.

- The peak value of pressure is at the stagnation point. As the flow expands further, an obvious drop in pressure is observed. The flow first expands along the spherical nose cap region. There is a change in geometry at the nose cap junction and the pressure increases due to positive gradient. Further the pressure remains almost constant in the cone region or decreases slightly.
- There is a sudden expansion in the cone-cylinder region. Thus the pressure falls sharply at the junction. The pressure is regained after the junction and the pressure suddenly jumps, thus indicating an ultrasonic shock from Mach number 0.7 to 0.95. As the Mach number increases, the expansion of flow increases. Flow separation does not take place for low Mach numbers in the transonic regime and there is a short separation for Mach numbers in the range 0.85 to 0.9. It can be seen in Fig. 4 and Fig. 5 that flow separation does not take place when the Mach number is between 1.0 and 1.2.

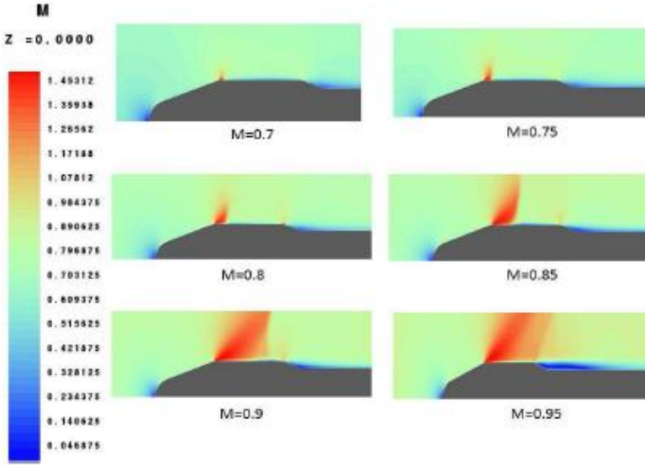


Fig. 4. Mach number distribution over heat shield

B. Separation Length

- As discussed above, there does not exist considerable flow separation in the low Mach number flow in the transonic regime and short distance separation takes place for Mach numbers around 0.9. So it can be noticed in table 1 that the flow separation length is longer as Mach number increases and the shockwave moves in boattail region at Mach number 0.95.

C. Shock Strength

- The pressures from the downstream and upstream sides were noted from the CFD results for analysing the shock

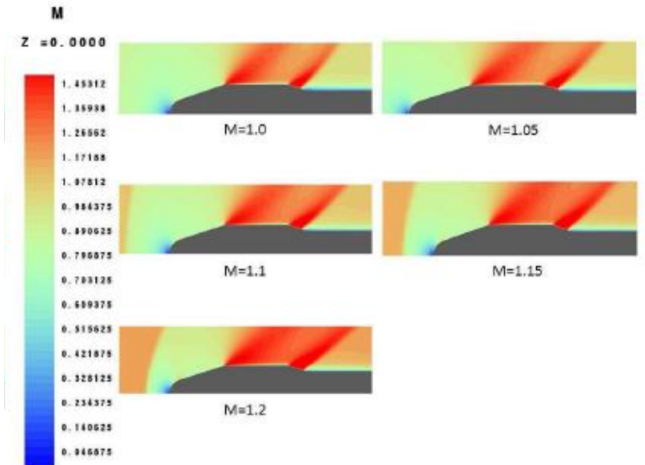


Fig. 5. Mach number distribution over heat shield

strength. The relation used for calculating the shock strength is given by following equation.

- From case study it is observed that as Mach number increases, the shock moves towards the aft body of the cylinder. For lower transonic Mach numbers, flow separation occurs and for higher Mach numbers in the transonic regime, shock is formed, but no shock induced separation occurs. Near the cone cylinder region, expansion waves are formed and they increase with the Mach number. It is also observed that as Mach number increases from 0.7 to 0.95, the shock strength reduces hence the shock waves strength also varies with the Mach number.

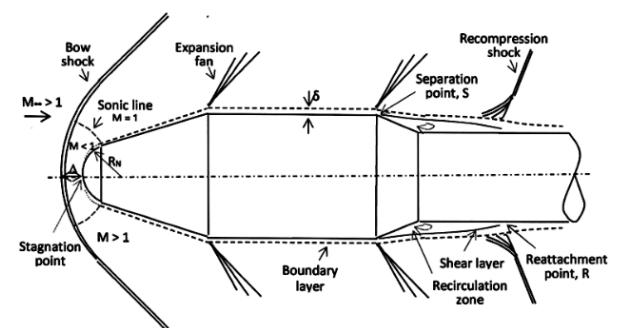


Fig. 6. Shock waves diagram

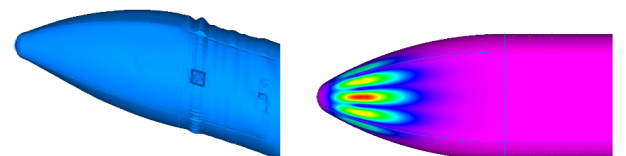


Fig. 7. Exaggerated deformed and 1st buckling mode shape at Max Q-alpha.

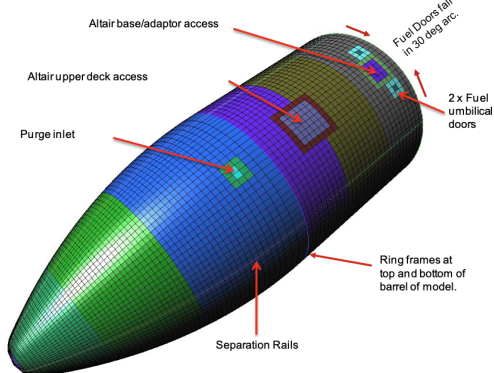


Fig. 8. Payload shroud PS-02 finite element model.

D. Payload Fairing Requirement

Requirements for the Structural Concept studies were extracted from the Ares V vehicle requirements. The remaining requirements could be identified as sub- sets of the following five categories.

- Payload protection and environmental control (Ground, launch and flight ops)
- Payload access (During integration and on-pad)
- Structural integrity (For all ground, launch and flight environments – includes inertial, aerodynamic, vibration, thermal and acoustic loads)
- Separation from launch vehicle (As commanded)
- System Telemetry (Including Structural Health Monitoring (SHM))

IV. ADAPTOR GEOMETRY AND DESIGN

The adapters considered in this work are made of a carbon fabric/epoxy composite material in the form of truncated conical or polyhedral shells as shown in Fig. 9. In these designs, the adapters do not have a bottom stiffening ring and are jointed to a launch vehicle at several supports. The adapters have cut-outs made between the points of support (see Fig.9). The shells are assembled of trapezoidshaped segments of a carbon fabric/epoxy prepreg and cured using vacuum bagging process. The top stiffening rings (see Fig. 10) are designed to accommodate the payload that is attached to the adapter. At the bottom, the adapter is jointed to the launcher structure through the fittings shown in Fig. 10. The spacecraft installed on the rocket launcher is shown in Fig. 11.

V. BUCKLING AND VIBRATIONS ANALYSIS

The main loadings are exerted on the adapter at the orbital injection leg. The intensity of these loads is determined by the mass of the payload and maximum values of the axial and transverse g-loads. In this work, finite-element buckling analyses were performed for the adapters subjected to axial compressive load and bending moment.

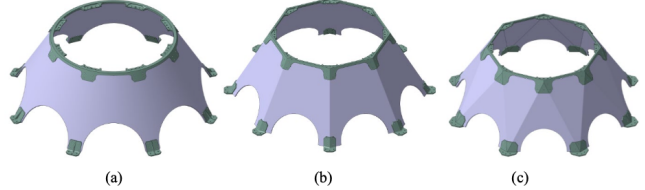


Fig. 9. Adapter designs: (a) truncated conical shell; (b) truncated octagonal pyramid with trapezoid facets; (c) truncated octagonal pyramid with triangular facets.

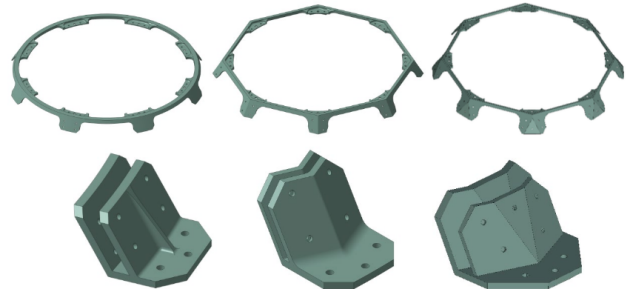


Fig. 10. Top stiffening rings and bottom fittings.

The diameters of the top, D_1 and bottom, D_2 bases of the shells are 1.2 and 2 m, respectively, and the height, H is 0.65 m. The carbon fiber reinforced plastic has the following characteristics: $E_1=70$ GPa, $E_2=70$ GPa, $G_{12}=5$ GPa, $v_{12}=0.31$, $v_{21}=0.31$, $\rho=1550$ kg/m³.

The effects of the shell thickness, and depth of the cut-outs,L on the critical loads have been investigated. The thicknesses of the shells were varied from 5 to 10 mm. The depth of the cut-outs ranged from 150 to 400 mm. For each combination of these structural parameters, the critical values of axial load and bending moment have been found. The values of critical axial load are presented in Tables 1, 2, and 3. The typical buckling mode shapes of the adapters under axial compression are shown in Fig. 16. The values of the critical buckling bending moments are presented in Tables 4, 5, and 6. Typical buckling mode shapes of the adapters under bending moment are shown in Fig. 20.

In addition to buckling analyses, the fundamental axial and transverse vibration frequencies have been calculated for the adapters with the payload attached. The payload mass was 3000 kg with the center of mass located at 2 m from the top base of the adapter. These characteristics are used to assess the axial and transverse stiffness of the adapter. The effects of the shell thickness and the size of the cut-outs on the fundamental frequency have been investigated using the finite-element analyses. The fundamental frequencies of axial vibrations are presented in Tables 7, 8, and 9. Typical axial vibration mode shapes are shown in Fig. 24.

The fundamental frequencies of transverse vibrations are presented in Tables 10, 11, and 12. Typical transverse vibration mode shapes are shown in Fig. 28 .

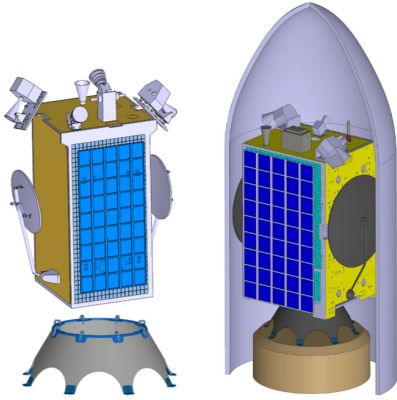


Fig. 11. Spacecraft assembly.

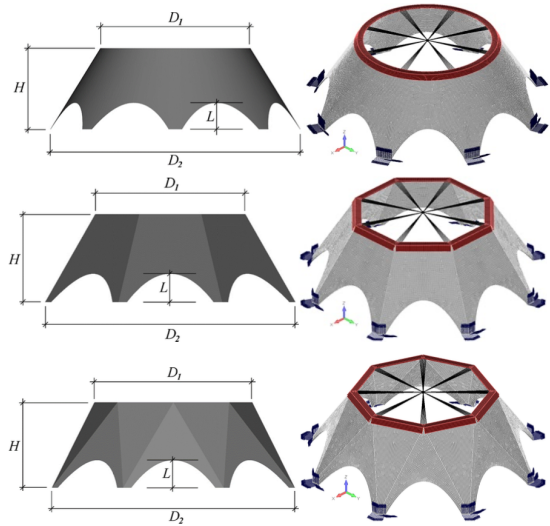


Fig. 12. Finite-element models of the adapters.

VI. CONCLUSIONS

In this work, new designs of the composite adapters are proposed and analysed. The adapters are made of a carbon fabric/epoxy composite material in the form of truncated conical or polyhedral shells. In these designs, the shells of the adapters have cut-outs. The adapters do not have a bottom stiffening ring and are jointed to a launch vehicle at a number of supports.

The finite-element models of the adapters were created in MSC Nastran. The finite-element buckling analyses were performed for the adapters subjected to axial compressive load and bending moment. The fundamental axial and transverse vibration frequencies have been calculated for the adapters with the payload attached. The effects of the shell thickness and the size of the cut-outs on the critical loads and on the fundamental frequencies were investigated.

The computational results showed that the designs of the adapters proposed in this work have considerable stiffness

h , mm	$L=150$ mm	$L=200$ mm	$L=250$ mm	$L=300$ mm	$L=350$ mm	$L=400$ mm
5	1039.5	849.4	693.5	566.3	460.6	366.7
6	1620.2	1327.4	1081.3	878.2	709.4	561.3
7	2302.9	1951.4	1585.9	1282.2	1030.4	811.6
8	3047.2	2700.9	2219.8	1787.7	1431.1	1123.6
9	3912.6	3464.3	2994.7	2404.3	1919.1	1503.2
10	4912.2	4336.2	3840.4	3140.9	2501.7	1956.2

Fig. 13. Table 1: Critical axial loads (kN) for the adapters in the form of conical shell

h , mm	$L=150$ mm	$L=200$ mm	$L=250$ mm	$L=300$ mm	$L=350$ mm	$L=400$ mm
5	365.8	361.1	362.3	370.9	388.1	416.3
6	625.9	617.3	618.8	632.3	659.6	705.4
7	983.6	969.3	970.4	989.3	1028.6	1095.2
8	1452.9	1430.5	1430.1	1454.4	1506.7	1596.4
9	2047.7	2014.3	2010.9	2040.1	2105.8	2220.1
10	2782.0	2734.2	2725.7	2759.1	2838.3	2977.9

Fig. 14. Table 2: Critical axial loads (kN) for the adapters in the form of truncated octagonal pyramid with trapezoid facets.

and can be considered as prospective structural elements. The finite-element models created for the structures under consideration allow the design analyses to be performed. Based on these analyses, the structural parameters of the adapters can be determined considering design requirements and constraints related to the stiffness and structural stability

h	$L=150 \text{ mm}$	$L=200 \text{ mm}$	$L=250 \text{ mm}$	$L=300 \text{ mm}$	$L=350 \text{ mm}$	$L=400 \text{ mm}$
5 mm	1231.4	1205.3	1236.5	1303.6	1135.7	700.2
6 mm	1958.2	1893.0	1902.8	1959.3	1520.0	974.3
7 mm	2910.6	2780.3	2757.5	2790.1	1934.0	1285.6
8 mm	4117.4	3897.6	3821.6	3529.4	2390.3	1638.2
9 mm	5606.8	5270.1	5120.4	4208.8	2896.5	2036.7
10 mm	7313.5	6922.2	6675.7	4948.8	3459.4	2486.0

Fig. 15. Table 3 : Critical axial loads (kN) for the adapters in the form of a truncated octagonal pyramid with triangular facets.

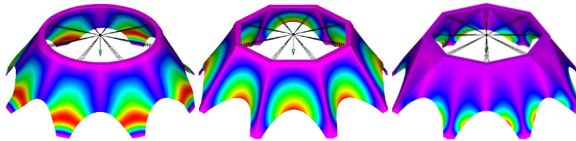


Fig. 16. Typical buckling mode shapes of the adapters under axial compression.

$h, \text{ mm}$	$L=150 \text{ mm}$	$L=200 \text{ mm}$	$L=250 \text{ mm}$	$L=300 \text{ mm}$	$L=350 \text{ mm}$	$L=400 \text{ mm}$
5	505.2	423.4	350.8	287.5	232.9	184.6
6	789.9	655.1	538.8	440.3	355.3	280.3
7	1150.4	952.2	780.5	636.6	511.7	402.6
8	1559.3	1318.6	1081.8	881.3	705.9	554.2
9	2011.4	1737.7	1448.1	1179.4	941.2	738.3
10	2530.8	2190.8	1880.9	1533.9	1221.2	957.6

Fig. 17. Table 4: Critical bending moments (kN m) for the adapters in the form of conical shell.

$h, \text{ mm}$	$L=150 \text{ mm}$	$L=200 \text{ mm}$	$L=250 \text{ mm}$	$L=300 \text{ mm}$	$L=350 \text{ mm}$	$L=400 \text{ mm}$
5	191.5	185.2	174.7	162.6	151.2	141.1
6	327.8	317.2	299.3	278.5	258.7	240.9
7	515.1	498.9	470.9	437.9	406.3	377.7
8	760.6	737.6	696.4	647.1	599.4	555.9
9	1071.3	1039.5	982.1	911.7	842.9	779.9
10	1454.3	1412.3	1334.4	1237.1	1141.7	1053.8

Fig. 18. Table 5: Critical bending moments (kN m) for the adapters in the form of truncated octagonal pyramid with trapezoid facets..

h	$L=150 \text{ mm}$	$L=200 \text{ mm}$	$L=250 \text{ mm}$	$L=300 \text{ mm}$	$L=350 \text{ mm}$	$L=400 \text{ mm}$
5 mm	482.3	480.0	484.5	489.7	397.4	264.6
6 mm	810.5	775.5	762.3	716.34	542.7	369.8
7 mm	1215.0	1154.5	1111.0	954.9	709.5	493.8
8 mm	1709.9	1610.1	1485.5	1220.7	900.7	638.6
9 mm	2298.7	2132.3	1895.5	1517.8	1119.0	806.4
10 mm	2984.7	2721.1	2349.9	1849.8	1367.2	999.6

Fig. 19. Table 6: Critical bending moments (kN m) for the adapters in the form of truncated octagonal pyramid with triangular facets.

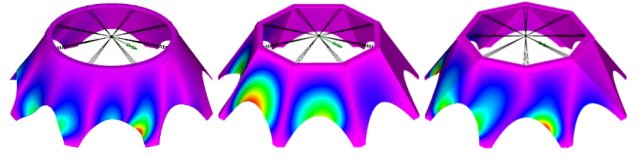


Fig. 20. The typical buckling mode shapes of the adapters under bending moment

$h, \text{ mm}$	$L=150 \text{ mm}$	$L=200 \text{ mm}$	$L=250 \text{ mm}$	$L=300 \text{ mm}$	$L=350 \text{ mm}$	$L=400 \text{ mm}$
5	75.4	74.5	73.4	72.2	70.8	69.2
6	83.2	82.1	80.8	79.3	77.6	75.9
7	90.2	88.9	87.5	85.8	83.9	81.9
8	96.8	95.4	93.7	91.8	89.8	87.6
9	102.9	101.4	99.6	97.5	95.2	92.9
10	108.8	107.1	105.1	102.8	100.4	97.9

Fig. 21. Table 7: Fundamental frequencies of axial vibrations (Hz) for the adapters in the form of conical shell.

$h, \text{ mm}$	$L=150 \text{ mm}$	$L=200 \text{ mm}$	$L=250 \text{ mm}$	$L=300 \text{ mm}$	$L=350 \text{ mm}$	$L=400 \text{ mm}$
5	61.8	63.9	67.2	72.1	70.9	68.7
6	73.7	76.1	79.9	79.9	77.5	75.1
7	85.4	88.1	88.6	86.1	83.5	80.9
8	96.9	96.9	94.5	91.8	89.1	86.4
9	104.9	102.6	100.1	97.3	94.4	91.5
10	110.7	107.9	105.3	102.4	99.3	96.3

Fig. 22. Table 8: Fundamental frequencies of axial vibrations (Hz) for the adapters in the form of truncated octagonal pyramid with trapezoid facets.

$h, \text{ mm}$	$L=150 \text{ mm}$	$L=200 \text{ mm}$	$L=250 \text{ mm}$	$L=300 \text{ mm}$	$L=350 \text{ mm}$	$L=400 \text{ mm}$
5	78.0	76.1	73.9	71.3	68.4	64.8
6	85.2	83.2	80.8	78.0	74.8	70.9
7	91.8	89.7	87.1	84.1	80.6	76.6
8	97.9	95.7	93.0	89.8	86.2	81.9
9	103.7	101.3	98.5	95.2	91.3	86.9
10	109.2	106.7	103.7	100.3	96.3	91.7

Fig. 23. Table 9: Fundamental frequencies of axial vibrations (Hz) for the adapters in the form of truncated octagonal pyramid with triangular facets.

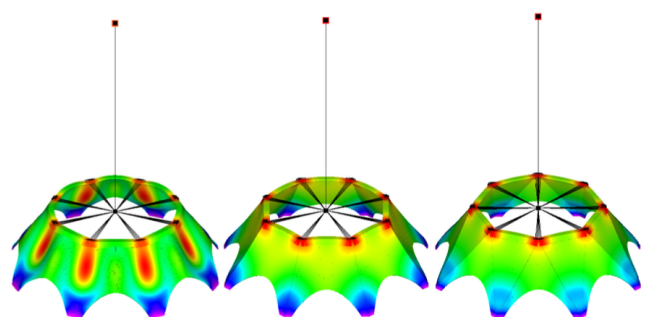


Fig. 24. The typical axial vibration mode shapes of the adapters.

h , mm	$L=150$ mm	$L=200$ mm	$L=250$ mm	$L=300$ mm	$L=350$ mm	$L=400$ mm
5	16.5	16.1	15.6	15.1	14.5	13.9
6	18.4	17.9	17.4	16.8	16.1	15.6
7	20.1	19.6	19.1	18.4	17.7	16.9
8	21.6	21.1	20.5	19.8	19.1	18.3
9	23.1	22.5	21.9	21.2	20.4	19.6
10	24.4	23.9	23.2	22.5	21.7	20.7

Fig. 25. Table 10: Fundamental frequencies of transverse vibrations (Hz) for the adapters in the form of conical shell.

h , mm	$L=150$ mm	$L=200$ mm	$L=250$ mm	$L=300$ mm	$L=350$ mm	$L=400$ mm
5	17.6	17.1	16.5	15.9	15.1	14.3
6	19.2	18.7	18.1	17.3	16.5	15.7
7	20.7	20.1	19.4	18.7	17.8	16.9
8	22.1	21.4	20.7	19.9	19.1	18.1
9	23.4	22.7	21.9	21.1	20.1	19.1
10	24.6	23.9	23.1	22.2	21.2	20.1

Fig. 26. Table 11: Fundamental frequencies of transverse vibrations (Hz) for the adapters in the form of truncated octagonal pyramid with trapezoid facets.

h	$L=150$ mm	$L=200$ mm	$L=250$ mm	$L=300$ mm	$L=350$ mm	$L=400$ mm
5 mm	16.1	15.7	15.3	14.8	14.1	13.3
6 mm	17.8	17.4	16.9	16.4	15.6	14.7
7 mm	19.4	19.0	18.5	17.8	17.0	16.0
8 mm	20.9	20.4	19.9	19.1	18.3	17.2
9 mm	22.3	21.8	21.2	20.4	19.5	18.3
10 mm	23.6	23.0	22.4	21.6	20.6	19.4

Fig. 27. Table 12: Fundamental frequencies of transverse vibrations (Hz) for the adapters in the form of truncated octagonal pyramid with triangular facets.

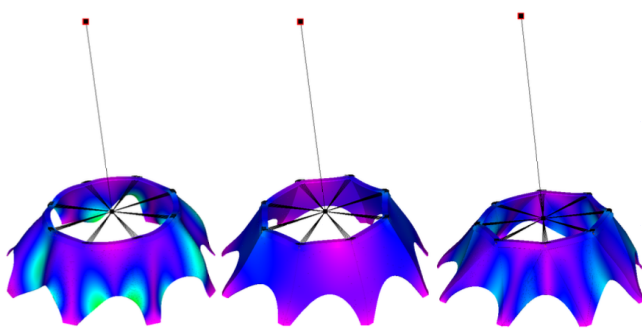


Fig. 28. The typical transverse vibration mode shapes of the adapters